Since January 2020 Elsevier has created a COVID-19 resource centre with free information in English and Mandarin on the novel coronavirus COVID-19. The COVID-19 resource centre is hosted on Elsevier Connect, the company's public news and information website.

Analytica Chimica Acta 1233 (2022) 340486

Contents lists available at ScienceDirect

Analytica Chimica Acta

journal homepage: www.elsevier.com/locate/aca

Magnetic/fluorescent dual-modal lateral flow immunoassay based on multifunctional nanobeads for rapid and accurate SARS-CoV-2 nucleocapsid protein detection

Zihao Xie [a,b], Shasha Feng [a,b], Fubin Pei [a,b], Mingzhu Xia [a], Qingli Hao [a], Bing Liu [b], Zhaoyang Tong [b], Jiang Wang [b], Wu Lei [a,*], Xihui Mu [b,**]

[a] School of Chemistry and Chemical Engineering, Nanjing University of Science and Technology, Nanjing, 210094, JiangSu, China
[b] State Key Laboratory of NBC Protection for Civilian, Beijing, 102205, China

HIGHLIGHTS

- A novel magnetic/fluorescent dual-modal LFIA for SARS-CoV-2 NP detection.
- Magnetic beads with double QD shells are used as labels for dual signal generation.
- The method has high quantitative analysis performance and can meet various needs.
- The dual-modal LFIA has outstanding specificity, reproducibility, and stability.

GRAPHICAL ABSTRACT

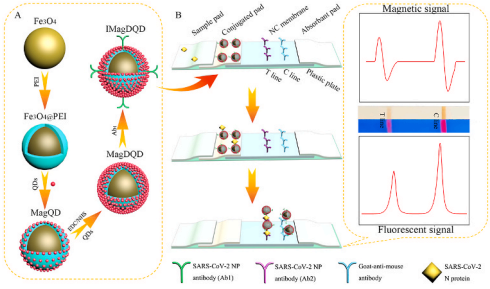

ARTICLE INFO

Keywords:
Multifunctional nanobeads
Magnetic/fluorescent dual-modal
Lateral flow immunoassay
SARS-CoV-2 nucleocapsid protein

ABSTRACT

The SARS-CoV-2 pandemic has posed a huge challenge to rapid and accurate diagnosis of SARS-CoV-2 in the early stage of infection. In this work, we developed a novel magnetic/fluorescent dual-modal lateral flow immunoassay (LFIA) based on multifunctional nanobeads for rapid and accurate determination of SARS-CoV-2 nucleocapsid protein (NP). The multifunctional nanobeads were fabricated by using polyethyleneimine (PEI) as a mediate shell to combine superparamagnetic Fe_3O_4 core with dual quantum dot shells (MagDQD). The core-shell structure of MagDQD label with high loading density of quantum dots (QDs) and superior magnetic content realized LFIA with dual quantitative analysis modal from the assemblies of individual single nanoparticles. The LFIA integrated the advantages of magnetic signal and fluorescent signal, resulting excellent accuracy for quantitative analysis and high elasticity of the overall detection. In addition, magnetic signal and fluorescent signal both had high sensitivity with the limit of detection (LOD) as 0.235 ng mL^{-1} and 0.012 ng mL^{-1}, respectively. The recovery rates of the methods in simulated saliva samples were 91.36%–103.60% (magnetic signal) and 94.39%–104.38% (fluorescent signal). The results indicate the method has a considerable potential to be an effective tool for diagnose SARS-CoV-2 in the early stage of infection.

* Corresponding author.
** Corresponding author.
E-mail addresses: leiwuhao@njust.edu.cn (W. Lei), mxh0511@sohu.com (X. Mu).

https://doi.org/10.1016/j.aca.2022.340486
Received 14 September 2022; Received in revised form 27 September 2022; Accepted 4 October 2022
Available online 7 October 2022

1. Introduction

The outbreak of coronavirus disease 19 (COVID-19), caused by the virus named severe acute respiratory syndrome coronavirus 2 (SARS-CoV-2), results the most influential pandemic in more than a century and is still impacting global societies [1,2]. According to World Health Organization (WHO) statistics, as of June 15, 2022, have been 534,495, 291 confirmed cases of COVID-19, including more than 6 million deaths. Most patients with SARS-CoV-2 infection would show several 'flu'-like symptoms such as fever, shortness of breath, dry and continuous cough, which could remind people to take countermeasures to avoid further transmission [3,4]. Unfortunately, there are other patients, who are asymptomatic or during the incubation period, have reportedly could spread the virus efficiently and may prove challenging for containing the pandemic [5,6]. Therefore, it is significant to sensitively and rapidly diagnose patients with SARS-CoV-2 in the early stage of infection.

There are three main categories strategies developed to diagnose SARS-CoV-2 in the global pandemic including nucleic acid test, antibody test, and antigen test [7]. Nucleic acid testing with real-time polymerase chain reaction (RT-PCR) is the primary method to diagnose COVID-19 [8]. Antibody detection and antigen detection have been great supplementary methods for containing SARS-CoV-2 due to the advantages of rapid and low-cost. However, SARS-CoV-2 specific antibodies like IgM and IgG could detect between 7 and 14 days after symptom onset, which may not be suitable for screening in the early stage of infection [9,10]. Thus, antigen detection is more suitable for early detection, especially nucleocapsid protein (NP) detection [11,12]. NP is a structure protein of SARS-CoV-2 virus [13]. Compared with other structure proteins, NP has high immunogenicity and is more abundantly expressed in vivo during infection [14,15]. Hence, NP is a suitable marker for diagnosing SARS-CoV-2 in early infection.

Enzyme-linked immunosorbent assay (Elisa) [16], chemiluminescence immunoassay (CLIA) [17], and electrochemical immunosensor [18,19], are current methods to detect SARS-CoV-2 NP. These methods have high sensitivity and quantification advantages. However, high requirements for skilled operators and time-consuming steps limit their application for large-scale screening. Compared with these methods, lateral flow immunoassay (LFIA) owns its unique advantages of short reaction time, low-cost detection, portability, and user-friendliness which are suitable for screening, on-site, and rapidity to diagnose SARS-CoV-2 [20,21]. However, the traditional colloidal gold nanoparticles (AuNPs)-based LFIA has poor quantitative ability, high false negative rates and limited sensitive, due to the absence of readout system and the single signal of colorimetric [22–24]. With the development of nanomaterials, many novel materials, such as quantum dots (QDs) [25,26], up-conversion luminescence materials [27], fluorescent microsphere [28], and magnetic nanobeads (MBs) [29] are used as labels in LFIA and greatly promote the development of LFIA and realizes the quantitative detection of LFIA. Due to the strong photostability, high quantum yield, and tunable fluorescent wavelength of QDs with a signal readout system for LFIA, the QDs-based LFIA could offer high sensitivity and quantitative analysis property [30]. However, the QDs-based LFIA also could only provide a single fluorescent signal, the detection result was easily influenced by the background color and complex environment [31,32]. Hence, it is attractive to introduce magnetic signal in the QDs-based LFIA, which can improve the quantitative analysis performance and anti-interference capability of the immunoassay. Compared with other nanotags with optical signal, MBs with magnetic signal are not affected by the background color and optical signals generated by field complex environmental samples [33]. By integrating the advantages of magnetic signal and fluorescent signal, the LFIA exhibits high sensitivity and excellent ability to conquer the interference from background color. In addition, dual-modal LFIA has a high flexibility of the overall detection due to the integration of two quantitative modals with different ranges of detection [34,35].

In this work, a novel dual-modal LFIA based on magnetic quantum dots with double QD shells (MagDQD) was fabricated for rapid and accurate detection of SARS-CoV-2 NP. The MagDQD was synthesized by electrostatic adsorption and EDC/NHS chemical. An electropositive PEI shell was introduced to combine a superparamagnetic Fe_3O_4 core with a large number of QDs. Based on the high loading density of QDs and superior magnetic content, MagDQD based LFIA realized dual signal readout modal with individual single nanolabel. With the combination of magnetic signal and fluorescent signal, the LFIA exhibited high quantitative analysis performance, and could meet various detection requirements. Thus, the dual-modal LFIA can be an effectively tool to rapid, sensitive, and accurate diagnose SARS-CoV-2.

2. Experimental section

2.1. Reagents and apparatus

Ethylene glycol (EG), Poly (4-styrenesulfonic acid-*co*-maleic acid, SS: MA = 3:1, w = 20000) sodium salt (PSSMA), and polyethyleneimine (PEI, M_w = 25000, 50% aqueous solution) were obtained from Aladdin Reagent Co., Ltd. (Shanghai, China). Carboxyl functionalized CdSe/ZnS QDs (catalog no. CdSe-MPA-625) were purchased from Mesolight Inc (Suzhou, China). 1-(3-Dimethylaminopropyl)-3-ethylcarbodiimide hydro (EDC), N-hydroxysulfosuccinimide sodium salt (sulfo-NHS), casein, 2-(N-morpholino) ethanesulfonic (MES), Sodium chloride (NaCl), sodium dihydrogen phosphate (NaH_2PO_4), disodium hydrogen phosphate (Na_2HPO_4), ferric chloride hexahydrate ($FeCl_3{\cdot}6H_2O$), Tween 20, glycine, sucrose, sodium acetate trihydrate ($NaAc{\cdot}3H_2O$), trehalose, and maltose were obtained from Sigma-Aldrich (USA). SARS-CoV-2 NP, SARS-CoV-2 NP antibody 2D3 (Ab_1), SARS-CoV-2 NP antibody 3F2 (Ab_2), goat anti mouse IgG, influenza A (Flu A, H1N1) NP, influenza B (Flu B) hemagglutinin, SARS-CoV-2 SP, SARS-CoV NP and middle east respiratory syndrome (MERS) NP were obtained from Shandong Langdu bio-sciences and technology Co., Ltd. (Shandong, China). Respiratory syncytial virus (RSV) glycoprotein was obtained from Beijing Yanbixin technology Co., Ltd. (Beijing, China). Lysis buffer was purchased from Beijing Biomed Gene technology Co., Ltd. Deionized water (18.2 MΩ cm, 25 °C) was used in all the experimental processes. Nitrocellulose membrane (NC membrane) (CN95, CN140), conjugated pad, sample pad, and absorbent pad were obtained from Millipore (St. Boston, MO, USA). Artificial saliva, polyvinyl pyrrolidone K-30 (PVP K-30), and bovine serum albumin (BSA) were obtained from Solarbio (China).

Transmission electron microscope (TEM) images were characterized by using a Tecnai G2 F30 S-TWIN transmission electron microscope (FEI, Netherlands). The magnetic property was measured from Lake-Shore7404 (USA). The fluorescent spectrum was obtained from FLS1000 Photoluminescence Spectrometer (Edinburgh Instruments, English). The zeta potential was measured by Zetasizer Nano ZS90 (Malvern, English). The magnetic signal was obtained from immunomagnetic biosensor testing system which was developed by our laboratory. The fluorescent signal was obtained from fluorescent detector FD-100 (Zuoan Technology Testing Co., China). BioDot XYZ3050 (BioDot Trading Shanghai Co., Ltd, China) dispense platform were used to spay antibody on NC membrane. BioDot CM4000 Strip cutting machine (BioDot Trading Shanghai Co. Ltd, China) was used to prepare the test trip.

2.2. Preparation of MagDQD

The synthesis route of the MagDQD composites was illustrated in Scheme 1A. At first, the 150 nm Fe_3O_4 nanoparticle were prepared by a modified solvothermal method [36]. In short, 1.25 g PSSMA, 1.35 g $FeCl_3{\cdot}6H_2O$, and 7.22 g $NaAc{\cdot}3H_2O$ were added in 50 mL EG and mixed fully under magnetic stirring. Then, the dark red solution was sealed in an autoclave and heated at 200 °C for 10 h. The black precipitates were magnetically collected and washed 3 times with deionized water and ethanol respectively, and then dried in vacuum at 60 °C for 12 h. The

particle size of Fe_3O_4 MBs was controlled by adjusting the amount of NaAc·$3H_2O$ added. Secondly, 100 mg Fe_3O_4 MBs was dispersed in 20 mL PEI aqueous solution (2.5 mg mL^{-1}) under sonication for 30 min. Then the Fe_3O_4@PEI MBs were washed 3 times with deionized water and ethanol respectively and magnetically collected. Subsequently, 20 mg Fe_3O_4@PEI MBs dispersed in 10 mL of water and add 140 μL CdSe/ZnS QDs (10 μM) and react for 1 h under sonication. In this process, numerous QDs would rapidly electrostatically self-assembled with Fe_3O_4@PEI MBs. The magnetic quantum dot (MagQD) was magnetically collected and redispersed in 10 mL MES solution (0.05 M borate buffer containing 0.5 M NaCl, pH 4.7). Then, 10 mg EDC, 10 mg NHS and 100 μL CdSe/ZnS QDs (10 μM) were added in and reacted 40 min under sonication. A great number of QDs would combine with MagQD by EDC/NHS chemical. Finally, the MagDQD were washed 3 times with deionized water and redispersed in deionized water for further use.

2.3. Preparation of immuno-MagDQD labels

20 mg MagDQD was dispersed in 10 mL MES solution by ultrasound for 15 min. Then 1 mg EDC and 1 mg NHS were added in the solution to react at room temperature for 0.5 h with sonication, followed by washing 3 times with phosphate-buffered saline (PBS, 0.01 M, PH = 7.2–7.4). Next, MagDQD was dispersed in 1 mL PBS and 500 μg Ab_1 was added in to react at 4 °C for 12 h with stirring. Then, the MagDQD was magnetically collected and blocked with 1 mL PBS (containing 1% BSA (w/v)) for 4 h with stirring. Finally, the prepared immuno-MagDQD (IMagDQD) was washed with PBST and dispersed in 40 mL release solution (0.01 M PBS containing 10% sucrose (w/v), 5% maltose (w/v), and 5% D-Trehalose anhydrous (w/v)) for further use.

2.4. Fabrication of the dual-modal LFIA based on MagDQD

The dual-modal LFIA based on MagDQD was consisted of sample pad, conjugated pad, middle pad, NC membrane and absorbent pad five parts. The sample pads were soaked in PBS (containing 4% Triton-100, 0.1% tween-20, and 0.1% PVP-30K (w/v)) for 1 h and then dried at 37 °C for 6 h. The conjugated pads were soaked in PBS (containing 0.1% tween-20, 1% BSA (w/v), and 5% sucrose (w/v)) for 1h and then dried at 37 °C for 6 h. Then, dropped 750 μL (0.5 mg mL^{-1}) MagDQD solution (dispersed in release solution) onto the conjugated pad (1 cm *15 cm), and freezing dried for further use. The middle pads were soaked in blocking buffer (0.01 M PBS containing 2.5% sucrose (w/v), 10 mg mL^{-1} casein, and 1 M NaCl) for 1 h and then dried at 37 °C for 6 h. The test (T) line and control (C) line were sprayed by Ab_2 (1.25 mg mL^{-1}) and goat anti mouse IgG (2 mg mL^{-1}) in PBS onto the NC membrane by BioDot XYZ3050 dispense platform at the amount of 1 mL cm^{-1}, respectively, and then dried at room temperature for 1 h. Finally, the plastic plate assembled with the sample pad, conjugated pad, middle pad, NC membrane, and absorbent pad were cut into 4 mm wide lateral strips by BioDot CM4000 Strip cutting machine for future use.

2.5. Detection of SARS-CoV-2 NP

A series of SARS-CoV-2 NP solutions with concentrations ranging from 0.05 ng mL^{-1} to 1000 ng mL^{-1} were prepared by using PBS. Then, 100 μL prepared solution was added onto the sample pad of the dual-modal LFIA. In addition, PBS was used as the blank sample. After 10 min, the magnetic signal was measured by the immunomagnetic biosensor and fluorescent signal was measured by the fluorescent detector FD-100.

2.6. Detection of simulated SARS-CoV-2 NP samples

Saliva samples spiked with SARS-CoV-2 NP were mixed 1:4 with lysis buffer to prepare SARS-CoV-2 NP solutions of known concentration. The SARS-CoV-2 NP solution (10 μL) was added in PBS (90 μL) and mixed for 15 min by stirring. After thoroughly mixed, the mixture was added onto the sample pad of the strips. After 10 min, the results could be quantitative analyzed by measuring magnetic signal and fluorescent signal.

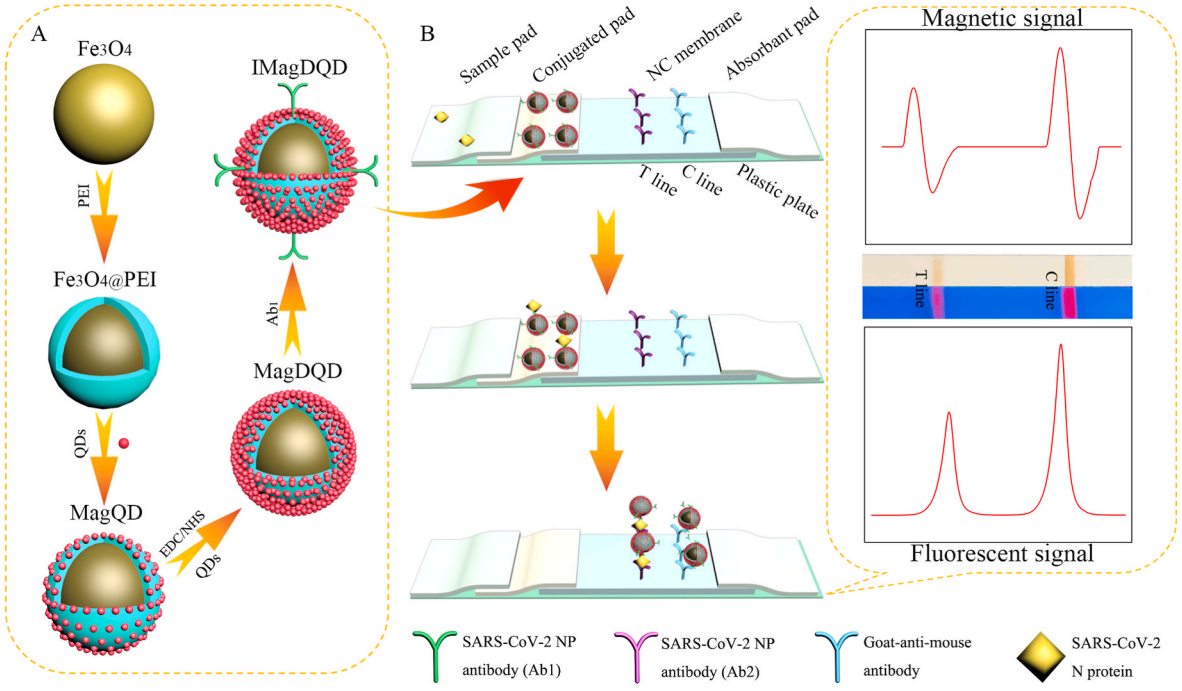

Scheme. 1. (A) Schematic illustration for the synthetic route and structure of antibody modified MagDQD label. (B) mechanism of dual-modal LFIA for SARS-CoV-2 NP detection.

3. Results and discussion

3.1. Characterization of MagDQD labels

In this work, a novel multifunctional nanocomposite with a 150 nm Fe_3O_4 core and numerous small QDs was synthesized, which had superior magnetic and fluorescent property. Scheme 1A illustrates the synthesis route of MagDQD, which is a modified layer-by-layer assembly strategy that involves the electrostatic adsorption and EDC/NHS chemistry. The Fe_3O_4 core were fabricated by the modified solvothermal method. The TEM image (Fig. 1A) shows that the Fe_3O_4 core with a homogeneous size of 150 nm were well-dispersed in the solution. Fig. 1B displays the TEM image of Fe_3O_4@PEI MBs, which indicates Fe_3O_4@PEI MBs have good dispersion and narrow distribution. Owing to the strong positive electricity of PEI, a great number of QDs were coated on the Fe_3O_4@PEI rapidly and firmly. Fig. 1C shows the structure of MagQD. After further reaction through EDC/NHS chemistry, massive QDs were coated on the surface of MagQD via the binding between the amino group of MagQD and the carboxyl group of QDs. Fig. 1D clearly shows that a great number of QDs were stably combined with MagQD to form the second QD shell. Fig. 1E shows the zeta potential results which can further demonstrate the structure of MagDQD was successfully prepared. After the PEI coated on Fe_3O_4, the zeta potential of Fe_3O_4@PEI increased from −37.8 mV to 40.8 mV. The zeta potential of MagQD decreased to 20.00 mV due to the absorption of negatively charged QDs (−7.93 mV). With the second QD shell combined with MagQD, the zeta potential of MagDQD decreased to 13.10 mV. The elemental mapping images (Fig. 1F) displays the elemental distribution of the MagDQD. Dense the elemental of Cd (blue), Se (purple), Zn (red), and S (orange) surrounded the Fe (yellow) and O (green) core.

3.2. Performance of MagDQD labels

Next, the magnetic property, fluorescent property, and stability of MagDQD were investigated. As shown in Fig. 2A, the saturation magnetization (MS) values of Fe_3O_4, Fe_3O_4@PEI, MagQD, and MagDQD were 62.51, 61.24, 54.57, and 47.86 emu g^{-1}, respectively. The MS values of the materials were decreased gradually due to the proportion of the Fe_3O_4 core was decreased gradually. But the MagDQD still had a good magnetization which can provide the magnetic signal for the detection of SARS-CoV-2 NP. Furthermore, the fluorescent spectra of Fe_3O_4, Fe_3O_4@PEI, MagQD, and MagDQD are shown in Fig. 2B. MagQD and MagDQD both exhibited excellent fluorescent property which had a narrow emission peak at 622 nm under a single UV light at 360 nm. And the fluorescent intensity of MagDQD was 1.7 times higher than MagQD due to the increasement of QDs content. The stability of MagDQD was tested in Fig. 2C. After stored at PBS for days, the fluorescent intensity of MagDQD remained stable, which proved that the MagDQD had a superior stability to be a label for dual-modal LFIA. Furthermore, the size of Fe_3O_4 core has a great influence on the property (size, fluorescent intensity, and magnetic intensity) of MagDQD. Three kinds of core with size of 100 nm, 150 nm, and 200 nm were used to synthesize MagDQD. The TEM of these MagDQD were shown in Figs. S1A–C. Fig. S1D shows that the MagDQD with bigger size of Fe_3O_4 core exhibited stronger magnetic value, which can output stronger magnetic signal. However, the MagDQD with 200 nm Fe_3O_4 core was limited by the weak fluorescent intensity, which would result weak fluorescent signal. Hence, the MagDQD with 150 nm Fe_3O_4 core was more suitable to build a dual-modal LFIA for SARS-CoV-2 NP detection.

In this work, the fluorescent intensity and zeta potential has detected with different amounts of QDs for second QDs layer (Fig. S2A). The fluorescent intensity of MagDQD was increased with the increasing of the QDs amounts. However, the zeta potential of MagDQD was decreased with the increasing of the QDs amounts, which was unfavorable to the stability of MagDQD. Hence, the MagDQD with 100 μL to form the second QDs layer was be chosen.

3.3. Principle of the dual-modal LFIA

The principle of the dual-modal LFIA is illustrated in Scheme 1B. The LFIA was built based on the formation of dual antibody immunosandwich format. The test sample was dropped onto the sample pad and flowed with the strip under the capillary action. The IMagDQD labels on conjugated pad were rapidly and specifically combined with SARS-CoV-2 NP to form the immunocomplexes. The immunocomplexes were captured by Ab_2 on T line. Subsequently, the free IMagDQD labels, which are not combined with SARS-CoV-2 NP, were captured by the goat anti mouse IgG on C line. After adding the samples for 10 min, the magnetic signal was measured by the immunomagnetic biosensor testing system, and the fluorescent signal was measured by the fluorescent detector FD-100. The concentration of SARS-CoV-2 NP could be quantitative analyzed by the ratio of the magnetic signal on T line to the magnetic signal on C line (Magnetic T/C) and the ratio of the fluorescent signal on T line to the fluorescent signal on C line (Fluorescent T/C).

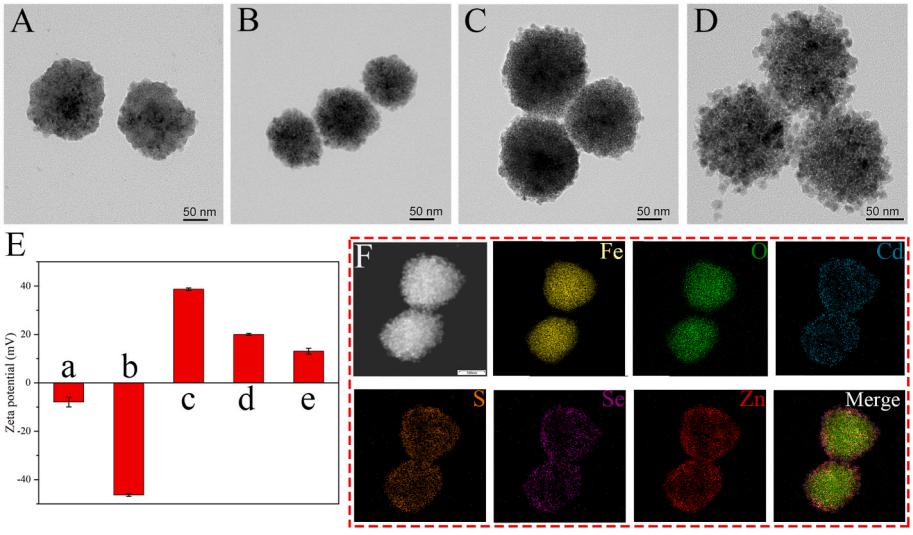

Fig. 1. Structural characterization of the synthesized MagDQD. TEM images of (A) Fe_3O_4 MBs, (B) Fe_3O_4@PEI MBs, (C) MagQD and (D) MagDQD. (E) The zeta potential of (a) QDs, (b) Fe_3O_4, (c) Fe_3O_4@PEI, (d) MagQD and (e) MagDQD. Error bar = SD, n = 3. (F) Elemental mapping images of MagDQD.

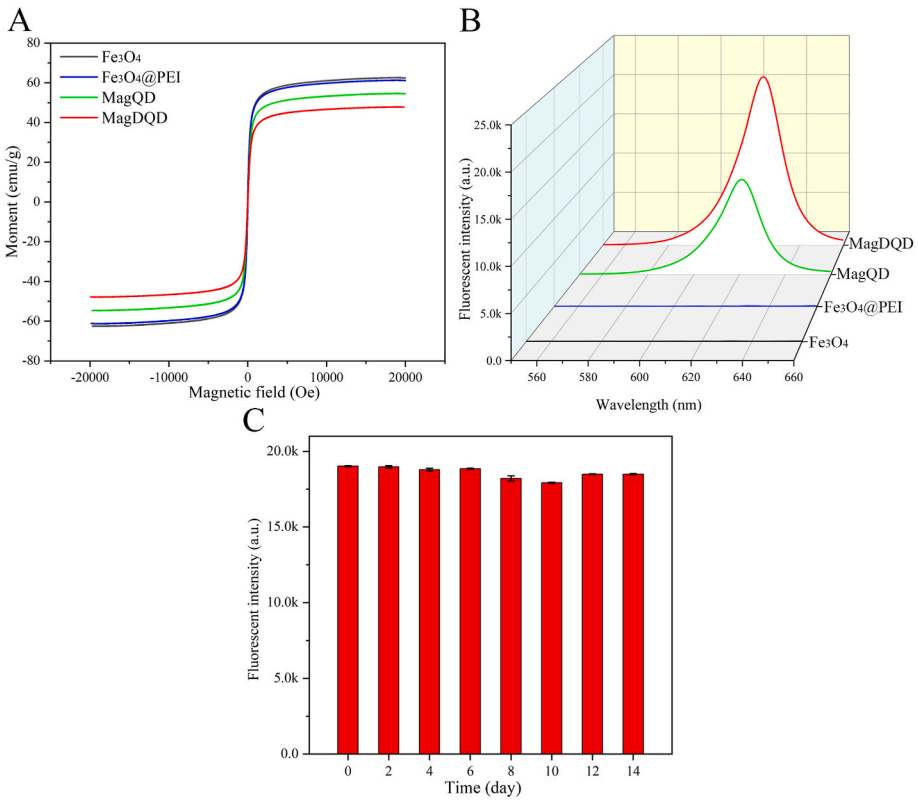

Fig. 2. (A) Magnetic property and (B) Fluorescence spectra of the Fe_3O_4, Fe_3O_4@PEI, MagQD and MagDQD. (C) Fluorescent intensities of MagDQD dispersed in PBS over storage time. Error bar = SD, n = 3.

3.4. Optimization of dual-modal LFIA

In order to improve the capability of the dual-modal LFIA strips, the MagDQD, synthesized by 3 kinds of Fe_3O_4 with different size, were used in the dual-modal LFIA and were well-optimized. As shown in Fig. 3A, the dual-modal LFIA with a Fe_3O_4 core size of 150 nm had the highest ratio of signal to noise (SNR, the value of SNR is calculated by the ratio of the positive signal to the negative signal [37]) of magnetic signal (magnetic SNR), and the SNR of fluorescent signal (fluorescent SNR) was just slightly inferior to the LFIA prepared by the MagDQD with a Fe_3O_4 core size of 100 nm. Thus, the dual-modal LFIA were fabricated based on the MagDQD with a 150 nm Fe_3O_4 core. As shown in Fig. S2A, the NC membrane types were optimized, and the results indicated the NC membrane type of CN95 is better than CN140. False positive has a great impact on the accuracy and sensitivity of the LFIA. To reduce the non-specific binding between the MagDQD labels with the antibody on T line to eliminate the false positive results, the casein was introduced into the blocking buffer. As show in Figs. S2C and D, under the blocking effect of casein, the magnetic T/C and the fluorescent T/C of negative sample were decreased significantly. This might be because the non-specific interaction between the IMagDQD with the antibody on NC membrane could be effectively blocked by macromolecular protein [38]. Fig. 3B reveals that the dual-modal LFIA blocked by 1 mg mL^{-1} casein had the highest magnetic SNR and fluorescent SNR. After optimization, the photograph and fluorescent image were shown in Fig. S2D, the T line of the blank sample was completely invisible by the naked eye in the natural light and the UV light, and the T line of the positive sample could be clearly observed.

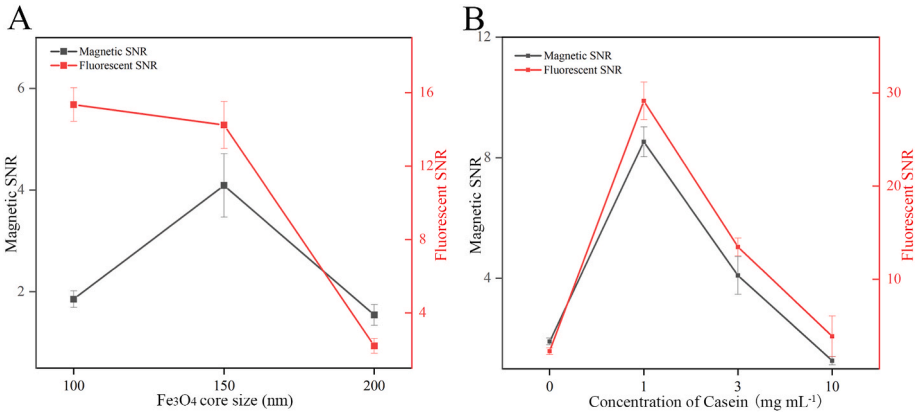

Fig. 3. Effects of experimental conditions on the magnetic SNR and fluorescent SNR: (A) Fe_3O_4 core size and (B) Concentration of casein in the blocking buffer. Positive sample was SARS-CoV-2 NP (50 ng mL^{-1}) dispersed in PBS, and the negative sample was PBS. Error bar = SD, n = 3.

3.5. Properties of the dual-modal LFIA for SARS-CoV-2 NP

After the optimization of the detection condition, the analytical performance of the dual-modal LFIA was examined with different concentration of the SARS-CoV-2 NP from 0.05 ng mL^{-1} to 1000 ng mL^{-1}. Fig. 4A shows the photograph of the dual-modal LFIA strips used for the detection of different concentration of the NP. With the concentration of the NP decreased, the brown color on T line became lighter, and could just be visualized the T line with a concentration of 1 ng mL^{-1}. The quantitative analysis of SARS-CoV-2 NP was performed by measuring the magnetic T/C. The calibration curves of the magnetic signal were constructed by the sigmoidal function and were displayed in Fig. 4B. The limit of detection (LOD) of the magnetic signal was determined to be 0.235 ng mL^{-1}, which was estimated by the IUPAC standard method (LOD, expressed as the concentration, cL is derived from the smallest measure, y_L. The value of y_L is given by the equation: $y_L = y_{blank} + 3SD_{blank}$, where y_{blank} is the mean of magnetic T/C of the blank group; SD_{blank} is the standard deviation) [39]. As shown in Fig. 4C, the detection results of the LFIA could be observed at the concentration of NP as low as 0.05 ng mL^{-1} by naked eyes under UV light. Fig. 4D showed that the LFIA also exhibited a wide detection range at the concentration 0.05–500 ng mL^{-1} by measuring fluorescent T/C. And the LOD of fluorescent signal was as low as 0.012 ng mL^{-1}. Notably, both fluorescent signal and magnetic signal were more sensitive than colorimetric signal. There are two different quantitative analysis modals with different range of detection by measuring magnetic signal and fluorescent signal, respectively. Combining magnetic signal and fluorescent signal, the dual-modal LFIA could provide a lower LOD and wider detection range for detecting SARS-CoV-2 NP than single signal. Compared with other assays for SARS-CoV-2 NP detection listed in Table S1, the dual-modal LFIA owned dual-signal readout capacity, sensitive property, and a wide detection range.

3.6. Specificity, reproducibility and stability

Furthermore, the specificity of the dual-modal LFIA were evaluated by testing several viruses (Flu A (H1N1), Flu B, MERS, SARS-CoV and RSV) and the spike protein of SARS-CoV-2 with a high concentration (500 ng mL^{-1}). As shown in Fig. 5A and B, the phenomenon of these viruses was similar to blank, and both magnetic signal and fluorescent signal were smaller than $y_{blank}+3SD_{blank}$. The results demonstrated that the dual-modal LFIA had a great specificity for detecting SARS-CoV-2 NP. In addition, the repeatability of the dual-modal LFIA was assessed by testing 10 independent samples. The results were exhibited in Fig. 5C. The relative standard deviation (RSD) of magnetic signal and fluorescence signal were 3.49% and 2.97% respectively, both lower than 5%, which showed that the method had a good reproducibility. The long-term stability of dual-modal LFIA strips was also accessed, and the results were displayed in Fig. 5D. The magnetic signal and the fluorescent signal were remained unchanged for 30 days after storing at 37 °C.

3.7. Simulated SARS-CoV-2 NP samples analysis

According to the previous experiments, these results indicated the excellent test performance, strong specificity, high repeatability, and good stability, which validated the feasibility of the dual-modal LFIA in practical application for detecting SARS-CoV-2 NP. To evaluate the property in actual sample detection of the dual-modal LFIA strips, recovery tests were conducted in simulated saliva samples. As exhibited in Table S2, the average recoveries of magnetic signal and fluorescent signal were 91.36%–103.60% and 94.39%–104.38% respectively, with the RSD of 1.23%–4.39%. The average recoveries and the low RSD proved that the dual-modal LFIA has considerable potential and prospect for the practical detection of SARS-CoV-2 NP.

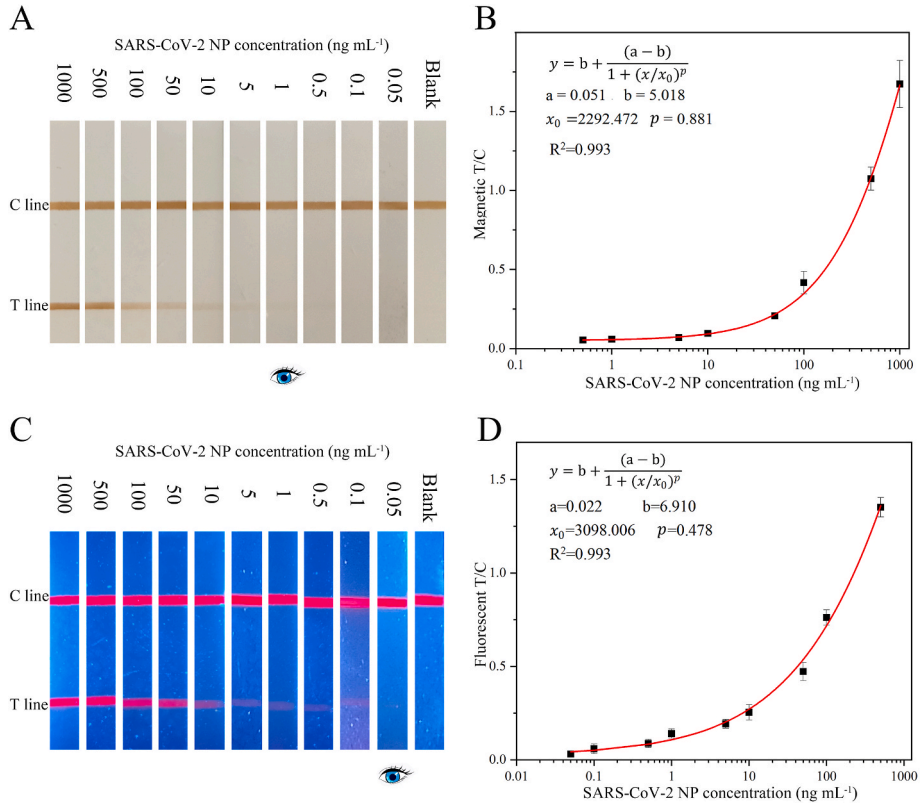

Fig. 4. Analytical performance of the dual-modal LFIA. Photograph (A) and fluorescent images (C) of the LFIA strips with different concentrations of SARS-CoV-2 NP (0.05–1000 ng mL^{-1}) and negative sample. Corresponding calibration curves for SARS-CoV-2 NP by measuring magnetic signal (B) and fluorescent signal (D). Error bar = SD, n = 5. Blank sample was PBS.

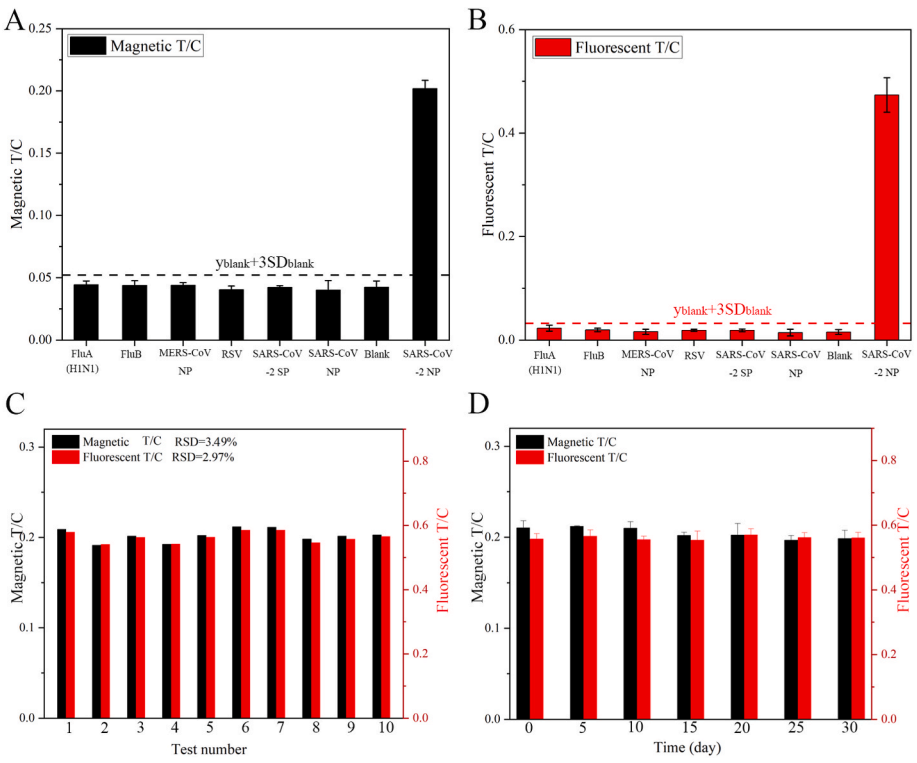

Fig. 5. Specificity of the dual-modal LFIA biosensor by measuring magnetic signal (A) and fluorescent signal (B). The concentration of SARS-CoV-2 NP was 50 ng mL^{-1} dispersed in PBS, and the blank sample was PBS. (C) Reproducibility of dual-modal LFIA strips for the detection of SARS-CoV-2 NP. (D) Long-term stability of dual-modal LFIA strips for detection of SARS-CoV-2 NP after store at 37 °C for 30 days. The sample was SARS-CoV-2 NP (50 ng mL^{-1}) dispersed in PBS. Error bar = SD, n = 3.

4. Conclusion

In summary, a dual-modal LFIA was developed for rapid and accurate determination of SARS-CoV-2 NP based on MagDQD label. The MagDQD, consisted of a 150 nm Fe_3O_4 core, an electropositive PEI shell and numerous QDs, owned excellent magnetic and fluorescent property. Compared with colorimetric signal, both of magnetic signal and fluorescent signal exhibited higher sensitivity with LODs at 0.235 ng mL^{-1} and 0.012 ng mL^{-1}, respectively. Taking advantages of the magnetic/fluorescent dual-signal, the novel LFIA provided accurate and sensitive dual-modal quantitative analysis for determination of SARS-CoV-2 NP within 10 min. Besides, the LFIA not only had excellent specificity, reproducibility, stability, but also exhibited satisfactory recoveries in saliva samples. Given the remarkable analysis performances of the dual-model immunoassay, the method has a great potential for clinical diagnosis of SARS-CoV-2.

CRediT authorship contribution statement

Zihao Xie: Conceptualization, Methodology, Data curation, Writing – original draft. **Shasha Feng:** Methodology, Investigation. **Fubin Pei:** Methodology, Investigation. **Mingzhu Xia:** Methodology, Formal analysis. **Qingli Hao:** Methodology, Investigation. **Bing Liu:** Formal analysis, Visualization. **Zhaoyang Tong:** Formal analysis, Investigation. **Jiang Wang:** Methodology, Investigation. **Wu Lei:** Formal analysis, Writing – review & editing. **Xihui Mu:** Formal analysis, Funding acquisition, Writing – review & editing.

Declaration of competing interest

The authors declare that they have no known competing financial interests or personal relationships that could have appeared to influence the work reported in this paper.

Data availability

Data will be made available on request.

Acknowledgments

The work was supported by the Foundation of State Key Laboratory of NBC Protection for Civilian (SKLNBC2020-07, SKLNBC2019-05) and National Natural Science Foundation of China (No. 51872140).

Appendix A. Supplementary data

Supplementary data to this article can be found online at https://doi.org/10.1016/j.aca.2022.340486.

References

[1] M. Heo, J.H. Jeong, S. Ju, S.J. Lee, Y.Y. Jeong, J.D. Lee, J.W. Yoo, Comparison of clinical features and outcomes between SARS-CoV-2 and non-SARS-CoV-2 respiratory viruses associated acute respiratory distress syndrome: retrospective analysis, J. Clin. Med. 11 (2022).
[2] N.K. Singh, P. Ray, A.F. Carlin, C. Magallanes, S.C. Morgan, L.C. Laurent, E. S. Aronoff-Spencer, D.A. Hall, Hitting the Diagnostic Sweet Spot: Point-of-care SARS-CoV-2 Salivary Antigen Testing with an Off-The-Shelf Glucometer, vol. 180, Biosensors & Bioelectronics, 2021.
[3] A.G. Harrison, T. Lin, P.H. Wang, Mechanisms of SARS-CoV-2 transmission and pathogenesis, Trends Immunol. 41 (2020) 1100–1115.
[4] P. Zhou, X.-L. Yang, X.-G. Wang, B. Hu, L. Zhang, W. Zhang, H.-R. Si, Y. Zhu, B. Li, C.-L. Huang, H.-D. Chen, J. Chen, Y. Luo, H. Guo, R.-D. Jiang, M.-Q. Liu, Y. Chen, X.-R. Shen, X. Wang, X.-S. Zheng, K. Zhao, Q.-J. Chen, F. Deng, L.-L. Liu, B. Yan, F.-X. Zhan, Y.-Y. Wang, G.-F. Xiao, Z.-L. Shi, A pneumonia outbreak associated with a new coronavirus of probable bat origin, Nature 579 (2020) 270–273.
[5] Q.-X. Long, X.-J. Tang, Q.-L. Shi, Q. Li, H.-J. Deng, J. Yuan, J.-L. Hu, W. Xu, Y. Zhang, F.-J. Lv, K. Su, F. Zhang, J. Gong, B. Wu, X.-M. Liu, J.-J. Li, J.-F. Qiu, J. Chen, A.-L. Huang, Clinical and immunological assessment of asymptomatic SARS-CoV-2 infections, Nat. Med. 26 (2020) 1200–1204.
[6] C. Rothe, M. Schunk, P. Sothmann, G. Bretzel, G. Froeschl, C. Wallrauch, T. Zimmer, V. Thiel, C. Janke, W. Guggemos, M. Seilmaier, C. Drosten, P. Vollmar, K. Zwirglmaier, S. Zange, R. Wolfel, M. Hoelscher, Transmission of 2019-nCoV infection from an asymptomatic contact in Germany, N. Engl. J. Med. 382 (2020) 970–971.

[7] B. Udugama, P. Kadhiresan, H.N. Kozlowski, A. Malekjahani, M. Osborne, V.Y. C. Li, H. Chen, S. Mubareka, J.B. Gubbay, W.C.W. Chan, Diagnosing COVID-19: the disease and tools for detection, ACS Nano 14 (2020) 3822–3835.
[8] Y. Fang, H. Zhang, J. Xie, M. Lin, L. Ying, P. Pang, W. Ji, Sensitivity of chest CT for COVID-19: comparison to RT-PCR, Radiology 296 (2020) E115–E117.
[9] B. Diao, K. Wen, J. Zhang, J. Chen, C. Han, Y.W. Chen, S.F. Wang, G.H. Deng, H. W. Zhou, Y.H. Wu, Accuracy of a nucleocapsid protein antigen rapid test in the diagnosis of SARS-CoV-2 infection, Clin. Microbiol. Infect. 27 (2021).
[10] H.-Y. Kim, J.-H. Lee, M.J. Kim, S.C. Park, M. Choi, W. Lee, K.B. Ku, B.T. Kim, E. Changkyun Park, H.G. Kim, S.I. Kim, Development of a SARS-CoV-2-specific biosensor for antigen detection using scFv-Fc fusion proteins, Biosens. Bioelectron. 175 (2021), 112868.
[11] W. Shao, M.R. Shurin, S.E. Wheeler, X. He, A. Star, Rapid detection of SARS-CoV-2 antigens using high-purity semiconducting single-walled carbon nanotube-based field-effect transistors, ACS Appl. Mater. Interfaces 13 (2021) 10321–10327.
[12] J. Li, P.B. Lillehoj, Microfluidic magneto immunosensor for rapid, high sensitivity measurements of SARS-CoV-2 nucleocapsid protein in serum, ACS Sens. 6 (2021) 1270–1278.
[13] W. Feng, A.M. Newbigging, C. Le, B. Pang, H. Peng, Y. Cao, J. Wu, G. Abbas, J. Song, D.-B. Wang, M. Cui, J. Tao, D.L. Tyrrell, X.-E. Zhang, H. Zhang, X.C. Le, Molecular diagnosis of COVID-19: challenges and research needs, Anal. Chem. 92 (2020) 10196–10209.
[14] C. Han, W. Li, Q. Li, W. Xing, H. Luo, H. Ji, X. Fang, Z. Luo, L. Zhang, CRISPR/Cas12a-Derived electrochemical aptasensor for ultrasensitive detection of COVID-19 nucleocapsid protein, Biosens. Bioelectron. 200 (2022), 113922.
[15] M.A. Ali, C.S. Hu, F. Zhang, S. Jahan, B. Yuan, M.S. Saleh, S.J. Gao, R. Panat, N protein-based ultrasensitive SARS-CoV-2 antibody detection in seconds via 3D nanoprinted, microarchitected array electrodes, J. Med. Virol. 94 (2022) 2067–2078.
[16] J. Liu, G. Ruan, W. Ma, Y. Sun, H. Yu, Z. Xu, C. Yu, H. Li, C.-w. Zhang, L. Li, Horseradish peroxidase-triggered direct in situ fluorescent immunoassay platform for sensing cardiac troponin I and SARS-CoV-2 nucleocapsid protein in serum, Biosens. Bioelectron. 198 (2022), 113823.
[17] A. Lyu, T. Jin, S. Wang, X. Huang, W. Zeng, R. Yang, H. Cui, Automatic label-free immunoassay with high sensitivity for rapid detection of SARS-CoV-2 nucleocapsid protein based on chemiluminescent magnetic beads, Sensor. Actuator. B Chem. 349 (2021), 130739.
[18] C. Karaman, B.B. Yola, O. Karaman, N. Atar, I. Polat, M.L. Yola, Sensitive sandwich-type electrochemical SARS-CoV-2 nucleocapsid protein immunosensor, Microchim. Acta 188 (2021).
[19] H.F. El Sharif, S.R. Dennison, M. Tully, S. Crossley, W. Mwangi, D. Bailey, S. P. Graham, S.M. Reddy, Evaluation of electropolymerized molecularly imprinted polymers (E-MIPs) on disposable electrodes for detection of SARS-CoV-2 in saliva, Anal. Chim. Acta 1206 (2022), 339777.
[20] P. Liang, Q. Guo, T. Zhao, C.-Y. Wen, Z. Tian, Y. Shang, J. Xing, Y. Jiang, J. Zeng, Ag nanoparticles with ultrathin Au shell-based lateral flow immunoassay for colorimetric and SERS dual-mode detection of SARS-CoV-2 IgG, Anal. Chem. 94 (2022) 8466–8473.
[21] Z.H. Chen, Z.G. Zhang, X.M. Zhai, Y.Y. Li, L. Lin, H. Zhao, L. Bian, P. Li, L. Yu, Y. S. Wu, G.F. Lin, Rapid and sensitive detection of anti-SARS-CoV-2 IgG, using lanthanide-doped nanoparticles-based lateral flow immunoassay, Anal. Chem. 92 (2020) 7226–7231.
[22] H. Li, B. Dong, L. Dou, W. Yu, X. Yu, K. Wen, Y. Ke, J. Shen, Z. Wang, Fluorescent lateral flow immunoassay for highly sensitive detection of eight anticoagulant rodenticides based on cadmium-free quantum dot-encapsulated nanospheres, Sensor. Actuator. B Chem. 324 (2020), 128771.
[23] Y. Zhou, Y. Chen, W. Liu, H. Fang, X. Li, L. Hou, Y. Liu, W. Lai, X. Huang, Y. Xiong, Development of a rapid and sensitive quantum dot nanobead-based double-antigen sandwich lateral flow immunoassay and its clinical performance for the detection of SARS-CoV-2 total antibodies, Sensor. Actuator. B Chem. 343 (2021), 130139.
[24] F. Gao, C. Lei, Y. Liu, H. Song, Y. Kong, J. Wan, C. Yu, Rational design of dendritic mesoporous silica nanoparticles' surface chemistry for quantum dot enrichment and an ultrasensitive lateral flow immunoassay, ACS Appl. Mater. Interfaces 13 (2021) 21507–21515.
[25] L. Ao, T. Liao, L. Huang, S. Lin, K. Xu, J. Ma, S. Qiu, X. Wang, Q. Zhang, Sensitive and simultaneous detection of multi-index lung cancer biomarkers by an NIR-II fluorescence lateral-flow immunoassay platform, Chem. Eng. J. 436 (2022), 135204.
[26] Z. Rong, Q. Wang, N. Sun, X. Jia, K. Wang, R. Xiao, S. Wang, Smartphone-based fluorescent lateral flow immunoassay platform for highly sensitive point-of-care detection of Zika virus nonstructural protein 1, Anal. Chim. Acta 1055 (2019) 140–147.
[27] J.C. Guo, S.Q. Chen, S.L. Tian, K. Liu, J. Ni, M. Zhao, Y.J. Kang, X. Ma, J.H. Guo, 5G-enabled Ultra-sensitive Fluorescence Sensor for Proactive Prognosis of COVID-19, vol. 181, Biosensors & Bioelectronics, 2021.
[28] J. Jiang, P. Luo, J. Liang, X. Shen, H. Lei, X. Li, A highly sensitive and quantitative time resolved fluorescent microspheres lateral flow immunoassay for streptomycin and dihydrostreptomycin in milk, honey, muscle, liver, and kidney, Anal. Chim. Acta 1192 (2022), 339360.
[29] Q. Bayin, L. Huang, C. Ren, Y. Fu, X. Ma, J. Guo, Anti-SARS-CoV-2 IgG and IgM detection with a GMR based LFIA system, Talanta 227 (2021), 122207.
[30] Y. Cao, Z. Chen, X. Li, Z. Li, G. Lin, T. Liu, Y. Wu, Dual-color quantum dot-loaded nanoparticles based lateral flow biosensor for the simultaneous detection of gastric cancer markers in a single test line, Anal. Chim. Acta 1218 (2022), 339998.
[31] J. Hu, Y.-Z. Jiang, M. Tang, L.-L. Wu, H.-y. Xie, Z.-L. Zhang, D.-W. Pang, Colorimetric-fluorescent-magnetic nanosphere-based multimodal assay platform for Salmonella detection, Anal. Chem. 91 (2019) 1178–1184.
[32] L. Su, H. Hu, Y. Tian, C. Jia, L. Wang, H. Zhang, J. Wang, D. Zhang, Highly sensitive colorimetric/surface-enhanced Raman spectroscopy immunoassay relying on a metallic core–shell Au/Au nanostar with clenbuterol as a target analyte, Anal. Chem. 93 (2021) 8362–8369.
[33] X.-H. Mu, H.-F. Liu, Z.-Y. Tong, B. Du, S. Liu, B. Liu, Z.-W. Liu, C. Gao, J. Wang, H. Dong, A new rapid detection method for ricin based on tunneling magnetoresistance biosensor, Sensor. Actuator. B Chem. 284 (2019) 638–649.
[34] L. Huang, J. Jin, L. Ao, C. Jiang, Y. Zhang, H.-M. Wen, J. Wang, H. Wang, J. Hu, Hierarchical plasmonic-fluorescent labels for highly sensitive lateral flow immunoassay with flexible dual-modal switching, ACS Appl. Mater. Interfaces 12 (2020) 58149–58160.
[35] H. Yang, Q. He, M. Lin, L. Ji, L. Zhang, H. Xiao, S. Li, Q. Li, X. Cui, S. Zhao, Multifunctional Au@Pt@Ag NPs with color-photothermal-Raman properties for multimodal lateral flow immunoassay, J. Hazard Mater. 435 (2022), 129082.
[36] J.N. Gao, X.Z. Ran, C.M. Shi, H.M. Cheng, T.M. Cheng, Y.P. Su, One-step solvothermal synthesis of highly water-soluble, negatively charged superparamagnetic Fe3O4 colloidal nanocrystal clusters, Nanoscale 5 (2013) 7026–7033.
[37] C.W. Wang, W.Z. Shen, Z. Rong, X.X. Liu, B. Gu, R. Xiao, S.Q. Wang, Layer-by-layer assembly of magnetic-core dual quantum dot-shell nanocomposites for fluorescence lateral flow detection of bacteria, Nanoscale 12 (2020) 795–807.
[38] J. Jia, L. Ao, Y. Luo, T. Liao, L. Huang, D. Zhuo, C. Jiang, J. Wang, J. Hu, Quantum dots assembly enhanced and dual-antigen sandwich structured lateral flow immunoassay of SARS-CoV-2 antibody with simultaneously high sensitivity and specificity, Biosens. Bioelectron. 198 (2022), 113810.
[39] C. Wang, R. Xiao, S. Wang, X. Yang, Z. Bai, X. Li, Z. Rong, B. Shen, S. Wang, Magnetic quantum dot based lateral flow assay biosensor for multiplex and sensitive detection of protein toxins in food samples, Biosens. Bioelectron. 146 (2019), 111754.